Lattice dynamics of the niobium (001) surface

E. Hulpke, M. Hüppauff, and D.-M. Smilgies
Max-Planck-Institut für Strömungsforschung, D-3400 Göttingen, Federal Republic of Germany

A. D. Kulkarni and F. W. de Wette
Department of Physics, University of Texas, Austin, Texas 78712-1081
(Received 29 March 1991)

In contrast to the reconstructing bcc (001) surfaces of molybdenum and tungsten, the niobium (001) surface is stable. From our helium-scattering experiments we find that the Nb(001) surface displays a regular surface phonon dispersion in spite of the pronounced phonon anomalies in bulk niobium that are due to strong electron-phonon interaction. We have modeled the surface dynamics of Nb(001) using a bulk-lattice-dynamical model that includes conventional central and angle-bending (three-body) interactions as well as electronic degrees of freedom. The latter are needed to account for the bulk phonon anomalies but are found to have little effect on the surface modes. This explains our experimental observation that the surface phonons do not exhibit an anomalous dispersion.

I. INTRODUCTION

The clean bcc (001) metal surfaces, other than W(001) and Mo(001), have not been studied very well so far. It is known from low-energy-electron-diffraction (LEED) experiments that some of these surfaces reconstruct [e.g., W(001) (Refs. 1 and 2) and Mo(001) (Ref. 2)], whereas some others are stable [for instance Nb(001) (Ref. 3) and Ta(001) (Ref. 4)]. In particular, the lattice dynamics of a stable bcc (001) surface such as Nb(001) has not yet been investigated.

Niobium is a very interesting material in itself: It has the highest superconducting transition temperature ($T_c = 9.3$ K) of all metals, indicating a strong electron-phonon interaction. In fact, strong anomalies in the bulk phonon dispersion of Nb have been observed by neutron scattering,[5] resulting in strong deviations from the regular sinusoidal shape of phonon-dispersion curves. In particular, one would expect that the parabolalike increase of the bulk transverse modes in the [100] and [110] directions would influence the dispersion of the Rayleigh mode, which is the most pronounced surface phonon mode.

Due to this anomalous behavior, simple force-constant models fail to describe the bulk dispersion relation unless force constants to a large number of neighbors are included.[5,6] It should be noted that these models are somewhat unphysical, since the electronic screening in a metal reduces the range of the interactions between the ion cores to a few lattice constants. The screening can be accounted for by calculating the electronic contribution to the dynamical matrix from the electronic band structure, as was successfully done by Varma and Weber[7] using a tight-binding approach. However, a phenomenological model introducing new electronic degrees of freedom[8,9] into the usual force-constant scheme proved to be very useful in the case of niobium. In this model, force constants up to third-nearest neighbors and electronic parameters up to second neighbors are used, which results in a much simpler analysis than in the tight-binding calculation, nevertheless yielding a very good agreement with the experimental bulk phonon data. We have therefore used the latter approach in our analysis of the surface phonons of Nb(001).

Our paper is organized as follows. In Sec. II we describe the experimental technique and the surface preparation. The results of the helium-atom scattering measurements are presented in Sec. III. Section IV provides a description of our lattice-dynamical model. Finally, our results are summarized in Sec. V.

II. EXPERIMENTAL PROCEDURE

The helium time-of-flight spectrometer consists of a nozzle beam source and a time-of-flight tube attached to the target chamber. Incoming and outgoing beam lines include a fixed angle of 101°. A monoenergetic He atom beam is produced in a nozzle expansion through an orifice 10 μm in diameter at a stagnation pressure of typically 100 bar. The nozzle temperature can be varied between 50 K and room temperature, resulting in beam energies between 15 and 70 meV. The beam is chopped for the time-of-flight measurements by a rotating disk with two slits. The sample can be manipulated in ultrahigh vacuum (typically 5×10^{-11} mbar) with respect to the polar axis varying the incident angle and the azimuth, in order to adjust for different directions on the surface. Detection of the scattered He atoms takes place in a magnetic mass spectrometer, and their final velocities are time-of-flight analyzed by a multichannel scaler. By the conservation laws of energy and quasimomentum, the phonon energy and wave vector can be determined.[10]

The niobium single crystal was provided by K. Schulze of the Max-Planck-Institut für Metallforschung in Stuttgart, FRG. A specimen of dimensions $20\times10\times1$ mm^3 was cut from the crystal by spark erosion and was then oriented and mechanically polished to within 0.1° of the (001) plane. After polishing, it needed to be annealed in vacuo at 2300 K for about 30 h until the first LEED

spots showed up. The main contaminants of the niobium specimen, as observed by Auger electron spectroscopy, were carbon, sulfur, and oxygen. Sulfur could be thermally desorbed by heating to temperatures of 2000 K. Carbon was removed by several cycles of exposing the surface to oxygen at 1500 K and heating it afterwards to 2300 K to remove the oxygen. However, it turned out to be a problem to eliminate the last traces of oxygen from the sample, which is characterized by a (3×1) LEED pattern. Such a structure has been observed previously on the chemically similar Ta(001) surface and was ascribed to a subsurface oxygen species.[4] Heating the sample to within 200 K of its melting point (2740 K) finally resulted in a clean surface. This heating procedure was repeated before each measurement.

III. EXPERIMENTAL RESULTS

After the sample preparation, angular distributions of the scattered He beam were recorded in order to measure the He diffraction patterns, which are presented in Fig. 1. Characteristics of a clean metal surface are a strong specular reflection and much weaker diffraction spots, since the He atoms are scattered from the electron density in the topmost layer, which is very smooth due to the delocalized nature of the electrons in a metal. The intensity of the first-order diffraction spots is indeed only 0.004 and 0.001 times that of the specular beam in the [100] and [110] directions, respectively. Higher-order diffraction spots are too weak to be seen aside from weak (20) spots at higher beam energies. In the [110] direction, the He diffraction pattern shown in Fig. 1(b) displays an additional diffraction peak close to the specular direction, the position of which does not depend on the incident beam energy. Obviously, this peak is a second specular reflection from a facet formed at a spot on the surface that had been slightly overheated during one of the cleaning cycles. The resulting deformation of the sample was due to an inhomogeneity of the crystal heating. However, this second specular reflection is a factor of 50 less in intensity than the main one. Therefore, it will not give rise to an error in the inelastic measurements, since the phonon signal from the corresponding facet will be weaker in intensity by the same factor. It should be mentioned that the He beam illuminates an area of 5 mm in diameter on the sample.

A scan of the diffraction peaks is also helpful for adjusting the crystal to within 0.5° (full width at half maximum of a diffraction peak) along the azimuth of the required high-symmetry direction for the surface phonon measurements. Time-of-flight spectra taken along both symmetry directions ([100] and [110]) reveal that there are two surface phonon modes on the Nb(001) surface that are separated in energy by less than 1 meV. In Fig. 2 a series of these spectra in the [110] azimuth are shown. Aside from the double-peaked phonon feature, a peak centered at zero energy transfer is also present in all these spectra, which is due to diffuse elastic scattering from surface defects. Since the energy separation of the two modes is close to the resolution limit of the apparatus, the incident beam energy had to be chosen carefully: As the relative He velocity spread is about 1% and nearly constant for all beam energies, the beam energy had to be sufficiently low to guarantee the required resolution. At the same time, it had to be high enough to ensure a reasonable value of the inelastic cross section. Therefore, it was necessary to use beams of several different energies to measure the surface phonon dispersion.

All phonon spectra were taken at a sample temperature of 900 K for the following reason: The main constituent of the residual gas in the scattering chamber is hydrogen, which is known to dissolve into bulk niobium[11] and does not form any ordered surface structures.[12,13] Since hydrogen is desorbed from the niobium lattice at about 750 K,[13] keeping the niobium crystal at 900 K during the He-scattering experiment guaranteed that no hydrogen uptake occurred. In this way, measuring times of typically half an hour could be achieved before the surface deteriorated and had to be cleaned again. Some test phonon spectra taken at room temperature showed no significant temperature effect on the surface phonons within our resolution of about 0.5 meV. However, after deliberate hydrogen exposure, the phonon signal decreased drastically, even though a (1×1) He diffraction

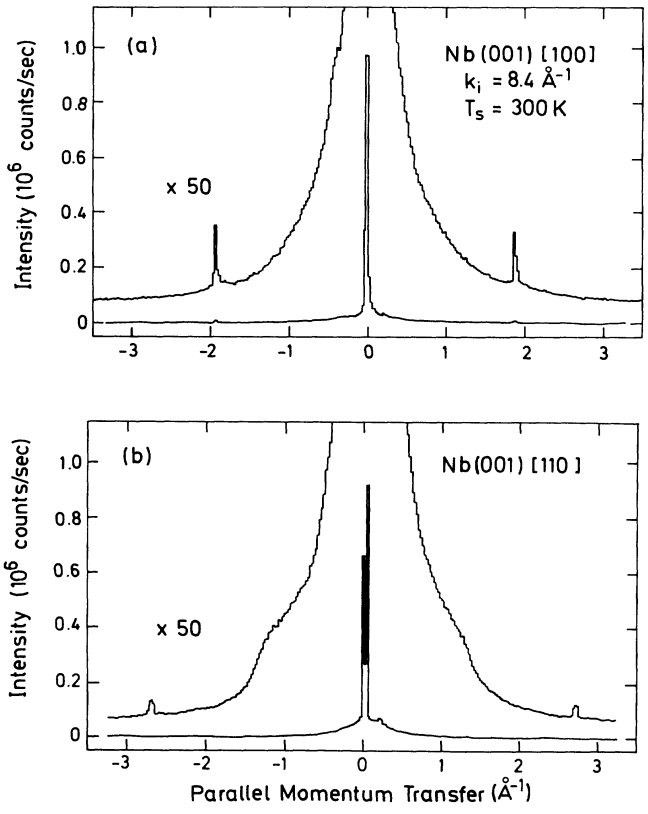

FIG. 1. Helium-atom diffraction from the clean Nb(001) surface in the (a) [100] and (b) [110] directions. Note that the first-order diffraction peaks are sharp and weak as compared to the specular reflection, which is typical for a smooth, well-ordered metal surface. The splitting of the specular reflection in (b) and also the small peak at about 0.2 Å^{-1} are due to macroscopic facets on the sample surface that had developed in the course of the heating cycles of the cleaning procedure.

pattern still persisted. Its intensity was, however, reduced as compared to that of the clean surface, indicating an increased amount of disorder in the topmost surface layer.

The measured surface-phonon-dispersion curves along the [100] ($\bar{\Gamma}\bar{X}$) and [110] ($\bar{\Gamma}\bar{M}$) directions are presented in Fig. 3. The two distinct modes observed close to $\bar{\Gamma}$ cannot be measured for wave vectors in the second half of the surface Brillouin zone. The mode at lower energies gradually diminishes in intensity compared to the mode at higher energies and cannot be detected for phonon wave vectors larger than 0.3 Å^{-1}. The higher-energy mode also becomes unobservable for wave vectors larger than 0.6 Å^{-1}. A possible explanation for this behavior is

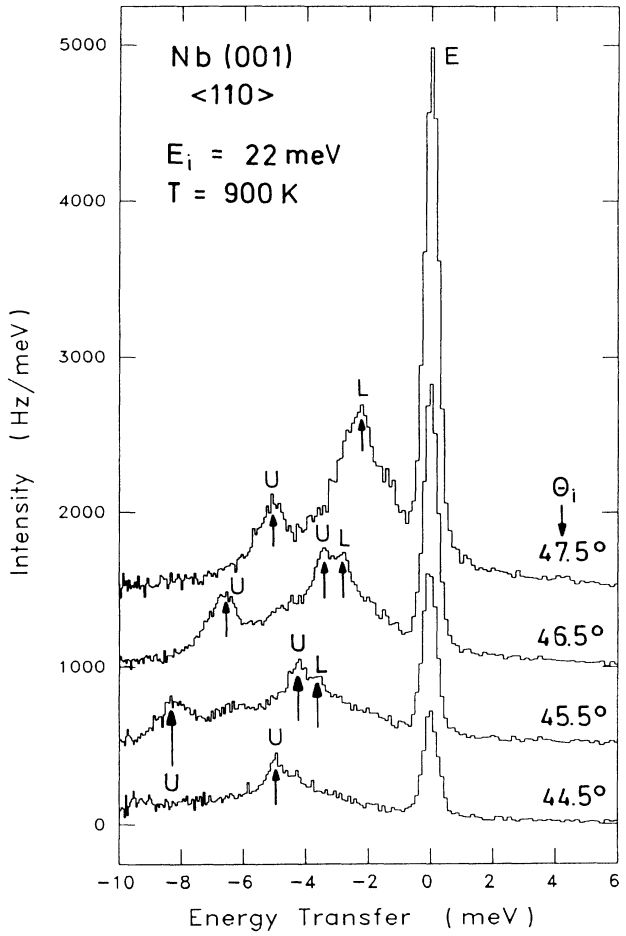

FIG. 2. Series of time-of-flight distributions measured along the [001] direction and converted to energy-loss spectra at a low incident beam energy of $E_i = 22$ meV. The strong peak at zero energy loss (E) is due to diffuse elastic scattering from surface defects. The peak at -2 meV in the topmost spectrum disperses upward in energy with decreasing incident angle Θ_i. For $\Theta_i < 47.5°$ it splits into a doublet of phonon inelastic peaks. The peak at lower energies (L) refers to the Rayleigh mode and weakens more rapidly with decreasing Θ_i than the second peak (U). The third inelastic peak at even larger energy losses refers to this second surface mode detected under different kinematic conditions (cf. Ref. 10).

that the surface, towards the end of the measurements, having suffered a number of heating cycles, had deteriorated and become rough. The temperatures needed to produce a clean surface cause a considerable evaporation of the topmost layers. Surface disorder might lead to a preferential attenuation of the surface modes, since these modes are strongly localized in the topmost surface layers (particularly in the vicinity of the zone boundaries) and will be strongly scattered by surface defects. Surface resonances, such as the upper energy mode, and surface-projected bulk modes are less affected by surface defects. It is, however, to be expected that the coupling of these latter modes to the impinging He atoms is strongly reduced by imperfections in the surface electron density due to defects, which will lead to a large deviation of the actual scattering potential from the one of an ideal surface.

Another experimental problem is that the measurements had to be performed at a surface temperature of 900 K, at which a considerable multiphonon background in the spectra (cf. Fig. 2) reduces the single phonon contribution. Hence it cannot be ruled out that the observability of surface phonons at higher wave vectors on the clean Nb(001) is hindered by experimental limitations due to the high chemical reactivity of this transition-metal surface and the difficulties in maintaining a clean surface.

From a comparison with the corresponding bulk phonon data,[5,6] we can assign polarization vectors to the observed surface phonons in the long-wavelength limit, i.e., close to the $\bar{\Gamma}$ point. Let us first examine the modes along [100]. The lowest surface mode lies just below the surface-projected transverse bulk band and can be identified as the Rayleigh mode. The surface mode at higher energies is located close to the longitudinal bulk band. It is embedded in this band and represents a surface resonance. Further comparison with the bulk modes reveals that the anomalous (parabolalike) increase of the transverse bulk mode along [ζ00] is not found for the Rayleigh mode along $\bar{\Gamma}\bar{X}$. The transverse bulk modes in this direction are degenerate. For temperatures ranging between 300 and 1000 K, these modes drop below the line $\omega = c_T q$ (cf. Ref. 6), where c_T denotes the transverse sound velocity and $q = (2\pi/a_0)\zeta$ the phonon wave vector. The measured surface phonon dispersion of the Rayleigh mode, however, lies slightly *above* the corresponding line. The same considerations hold for the $\bar{\Gamma}\bar{M}$ azimuth. However, they now refer to the transverse bulk mode of lower energy near Γ, since in the [$\zeta\zeta$0] direction the two transverse bulk modes are no longer degenerate. Note that in our scattering geometry, for symmetry reasons, the He atoms do not couple to the shear horizontal surface modes. Therefore, we do not detect the surface analogue of the second transverse bulk mode.

IV. LATTICE-DYNAMICAL MODEL

A. Bulk model

Our modeling of the measured surface vibrational modes is based on a lattice-dynamical model for bulk niobium. This model includes radial (α_i) and tangential

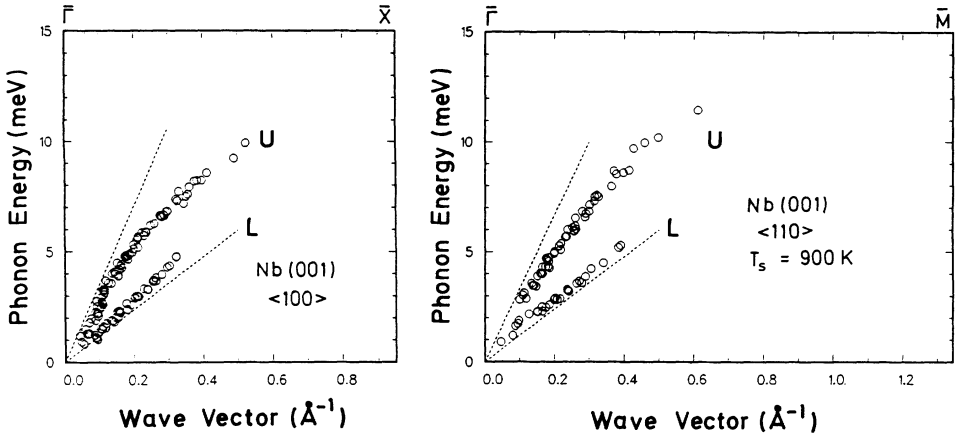

FIG. 3. Surface phonon dispersion on the clean Nb(001) surface along both high-symmetry directions at a sample temperature of 900 K. Two surface modes can be clearly resolved. The corresponding lower edges of the longitudinal and transverse surface projected bulk phonon bands are sketched as dashed lines. Close to $\bar{\Gamma}$ the slope of these curves corresponds to the appropriate sound velocities. From the behavior in the long-wavelength limit, the surface mode at lower energies (L) can be identified as the Rayleigh wave. The mode at higher energies (U) lies close to the longitudinal bulk band. It is embedded in the bulk band and thus represents a longitudinal resonance.

(β_i) force constants up to third neighbors (i.e., $i=1-3$), one-parameter angle-bending (three-body) interactions, and charge-fluctuation parameters of scalar and quadrupolar symmetry.

The dynamical model including the central and angle-bending interactions has been described in detail by Kulkarni and de Wette[14] and Kulkarni, de Wette, and Prade[15] for tungsten. The use of angle-bending interactions is a convenient way to account for the fact that niobium does not satisfy the Cauchy relation

$$c_{12}=c_{44}\ , \tag{1}$$

where c_{12} and c_{44} are components of the elastic tensor. This relation is necessarily obeyed if only central forces (satisfying the equilibrium condition) are involved and if, in addition, every particle occupies a site of inversion symmetry (cf. Ref. 16, p. 136). Bolef[17] reports that for niobium the Cauchy relation (1) is strongly violated: $c_{12}=13.45\times10^{11}$ dyn/cm^2 and $c_{44}=2.873\times10^{11}$ dyn/cm^2. The angle-bending interactions are also needed to obtain dynamical stability of the bcc structure (which is unstable under a broad class of central interactions; cf. Ref. 16, p. 152). For these reasons we include in our model an angle-bending force constant χ_1 defined as follows: Let p, i, and j be a triad of atoms such that i and j are first neighbors of p, and j is the second neighbor of i (cf. Fig. 4). Then χ_1 is the force constant associated with the angle at p such that the lattice potential energy contributed by one such angle is $(\frac{1}{2})\chi_1(a_0\delta\theta)^2$, where a_0 is the lattice constant of niobium (3.30 Å) and $\delta\theta$ is the change in the angle at p from its equilibrium value of 70.53°.

The charge-fluctuation parameters[8,9] are included in the model to account for the strong electron-phonon anomalies in the phonon-dispersion curves of niobium. Here we use the scalar (A_{1g} symmetry) and quadrupolar (T_{2g} symmetry) model proposed by Allen,[9] which includes 12 charge-fluctuation parameters. (For a pictorial representation of these charge fluctuations see Ref. 18.) From Allen's calculations it is seen (cf. Table II of Ref. 9) that out of the 12 charge-fluctuation parameters, only six, namely the scalar charge-fluctuation parameters up to second neighbors (ϕ_1,ϕ_2,A_1,A_2) and the quadrupolar charge-fluctuation parameters up to first neighbors (B_{1a},B_{1b}) have the largest effect on the bulk phonon-dispersion curves. We therefore include only these six charge-fluctuation parameters in our model. Since our model utilizes only six of the 12 charge-fluctuation parameters, the numerical values of these parameters given by Allen (in Table II of Ref. 9) cannot be used in our model. Moreover, Allen's model does not include angle-bending interactions. Due to these differences, we need to redetermine the numerical values of our model parameters by carrying out a least-squares fit to the bulk phonon-dispersion data.

Since our He-scattering experiments were performed at 900 K, our bulk dynamical model should ideally represent the experimental bulk phonon-dispersion data

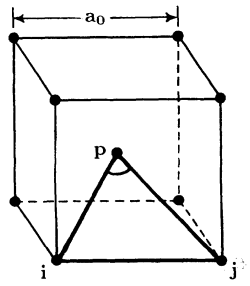

FIG. 4. Conventional unit cell of the niobium (bcc) lattice. The isosceles triangles similar to that formed by p,i,j are considered in the angle-bending interactions. The force constant χ_1 is associated with the angle at p.

at that temperature. These data were taken from Dederichs, Schober, and Sellmeyer.[6] However, since Ref. 6 contains extensive phonon-dispersion data at 296 K, we proceeded as follows: We obtained an initial set of model parameters by a least-squares fit to the 296 K data. By using this fit as a starting point, a subsequent fit—essentially a perturbation of the 296 K fit—was obtained by using the available 900 K data [see Fig. 5(a)]. The resulting parameter set is given in Table I, which shows that our values of the charge-fluctuation parameters are quite close to those found by Allen.[9] Thus the six charge-fluctuation parameters not included in our model do not have a significant effect on the bulk phonon-dispersion curves, and their exclusion is justified. Note that the violation of the Cauchy relation (1), which is a measure of the noncentral interactions, is

$$a_0(c_{44}-c_{12}) = 4(\beta_1+\beta_2+4\beta_3)+\tfrac{64}{9}\chi_1 + \frac{8(2A_1+A_2)^2}{1+8\phi_1+6\phi_2} - 32B_{1b}^2 = -6.58M \text{ THz}^2 , \quad (2)$$

which is within 15% of the experimental value[17] of $-5.73M$ THz^2 (M is the mass of the Nb atom). Also note that most of the contribution to Eq. (2) comes from the term $64\chi_1/9 = -4.62M$ THz^2, which justifies our use of the angle-bending force constant χ_1 to account for the violation of the Cauchy relation (1).

TABLE I. Fitted values of the lattice-dynamical model of bulk niobium. α_i, β_i ($i=1,2,3$), and χ_1 are expressed in THz^2, where M is the mass of the niobium atom. ϕ_1 and ϕ_2 are dimensionless. A_1, A_2, B_{1a}, and B_{1b} are expressed in THz.

$\alpha_1=4.619M$	$\beta_1=3.367M$
$\alpha_2=4.011M$	$\beta_2=-1.139M$
$\alpha_3=1.447M$	$\beta_3=-0.515M$
$\chi_1=-0.65M$	
$\phi_1=0.155$	$A_1=0.268M^{1/2}$
$\phi_2=0.130$	$A_2=-0.498M^{1/2}$
$B_{1a}=0.0352M^{1/2}$	$B_{1b}=0.287M^{1/2}$

The value of χ_1 was also dictated by the requirement that the dynamics of the Nb(001) slab be stable throughout the surface Brillouin zone: We found that the dynamics of the Nb(001) slab was especially prone to instabilities in the vicinity of the zone center of the sur-

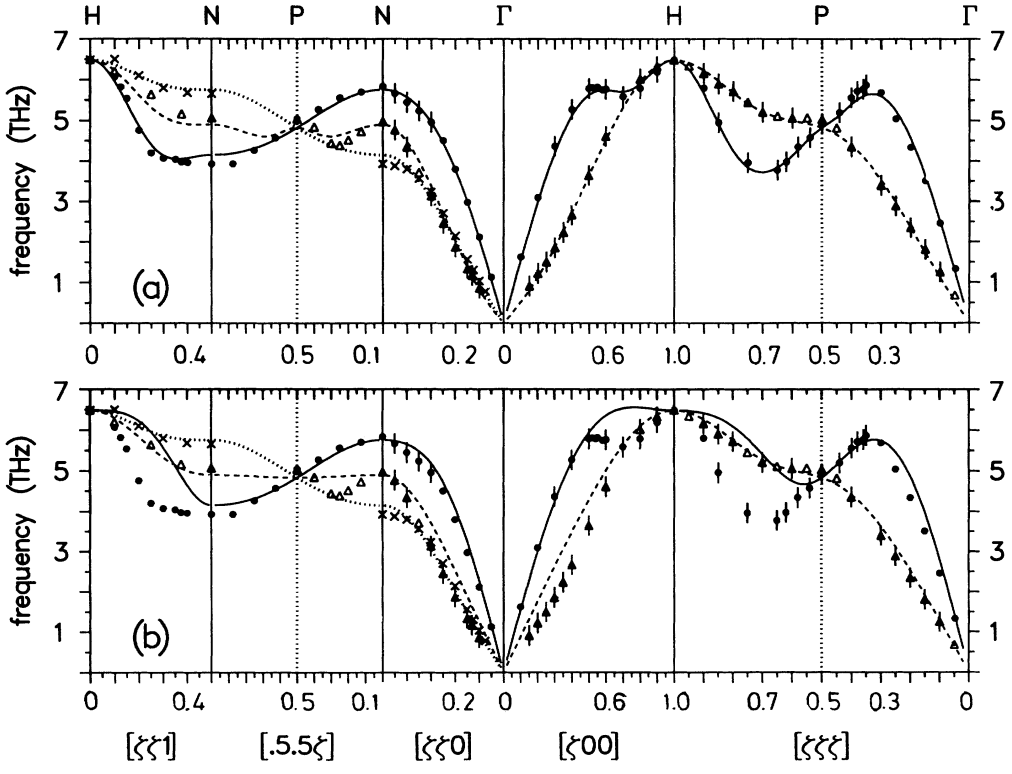

FIG. 5. (a) Bulk phonon data for niobium (Ref. 6) and the dispersion curves calculated from the lattice-dynamical model given in Table I. The solid and dashed lines represent the calculated longitudinal and transverse phonon-dispersion curves, respectively. The closed circles represent the longitudinal phonon data; the crosses and triangles denote the transverse phonon data. The data points with vertical bars correspond to the 900 K data. (The vertical bars are not error bars.) The dimensionless variable ζ is defined by $\zeta=q/(2\pi/a_0)$, where q is the phonon wave vector and a_0 the lattice constant of niobium. The numbers above $[\zeta\zeta 1]$, $[0.5,0.5\zeta]$, etc., are the values of ζ. (b) Same as in (a) except that the dispersion curves are calculated from the lattice-dynamical model given in Table I with all the charge-fluctuation parameters set equal to zero. The dispersion curves in this figure illustrate the importance of the charge-fluctuation parameters in accounting for the phonon anomalies.

face Brillouin zone, and the only way to remove this instability was to choose $\chi_1 \leq -0.65M$ THz^2. Thus χ_1 was taken to be $-0.65M$ THz^2 to stabilize the Nb(001) slab dynamics and to obtain the smallest discrepancy between Eq. (2) and the corresponding experimental value[17] of $-5.73M$ Thz^2. [The Nb(110) slab dynamics did not have these instability problems; it was found to be stable for the parameters of Table I.] In passing, we point out that our model does not satisfy the equilibrium condition; i.e., $\beta_1+\beta_2+4\beta_3=0.167M$ THz$^2 \neq 0$. However, the deviation ($0.167M$ THz^2) is small compared to the magnitudes of the tangential force constants β_i in our model (cf. Table I). Thus, in view of Eq. (2), it is seen that the β_i's contain small noncentral components.

In Fig. 5(a) we display the calculated bulk phonon-dispersion curves in the symmetry directions of the bulk Brillouin zone together with phonon-dispersion data from neutron-scattering experiments.[6] We draw attention to the following pronounced phonon anomalies in these curves: (i) The parabolalike increase (near Γ) of the lowest transverse dispersion curves in the $[\zeta 00]$ and $[\zeta\zeta 0]$ directions; (ii) dips in the longitudinal dispersion curves in the outer parts of the Brillouin zone in the $[\zeta 00]$ and $[\zeta\zeta\zeta]$ directions. As already mentioned, the charge-fluctuation parameters are included in the model to account for these anomalies. The effect of these parameters can be judged from Fig. 5(b), where the dispersion curves are obtained by setting all the charge-fluctuation parameters equal to zero. It is obvious that the agreement with the experimental data is substantially worse in the regions of the anomalies. We find that even the least-squares fit obtained by using just the force constants α_i, β_i ($i=1-3$), and χ_1 is not much different from the dispersion curves shown in Fig. 5(b). We have also carried out least-squares fits using additional force constants and angle-bending parameters. None of the additional parameters reproduce the phonon anomalies as well as the introduction of the charge-fluctuation parameters.

B. Surface modes

The surface modes and resonances of Nb(001) were determined by calculating the dynamics of a 51-layer slab of Nb(001). The use of such a thick slab enabled us to calculate the surface-projected density of states, which we used to locate all the surface modes and resonances predicted by our model. In order to be applicable to a slab (having more than one particle per unit cell), we had to generalize the charge-fluctuation model of Allen,[9] which was developed for one particle per unit cell. The generalization is described in Appendix A.

The best representation of the measured surface modes (Fig. 3) was obtained by modifying the second- and third-neighbor radial (α_2,α_3) and tangential (β_2,β_3) force constants *in* the surface layer, as shown in Table II. All other force constants were kept at their bulk values. It was found that the charge-fluctuation parameters at the surface do not appreciably influence the surface phonons; hence all those parameters were kept at their bulk values. The dispersion curves calculated using this model are shown in Fig. 6(a).

We need to comment here on the fact that the first-neighbor radial and tangential force constants between the surface and the second layers are not modified in the model. To understand this we refer to Eqs. (B1)–(B8) of Appendix B, which are taken from our earlier work on W(001).[15] These equations give analytical expressions for the dispersion of the Rayleigh ($SP_\perp$), longitudinal ($SP_\parallel$), and shear horizontal (SH) modes along $\bar{\Gamma}\bar{X}$ and $\bar{\Gamma}\bar{M}$, in a model in which only the top layer is allowed to vibrate, while all lower layers remain static. While admittedly this is a rather crude approximation, it is of great help in estimating which of the force constants are likely to have the most influence on a given surface mode.

Another fact to note is that without any force-constant changes at the surface, the $SP_\perp$ mode is *below* the corresponding experimental data, whereas the $SP_\parallel$ mode lies *above* the corresponding experimental data [see Fig. 6(b)].[19] Thus, in order to obtain agreement with experiment, $SP_\perp$ needs to be raised and $SP_\parallel$ needs to be lowered. With this in mind, consider Eqs. (B1)–(B8). It is seen immediately that changing the first-neighbor force constants will raise or lower both modes simultaneously, making it very difficult to modify these modes in opposite ways, by manipulating the first-neighbor force constants. Now consider the ways in which α_{2s}, α_{3s}, β_{2s}, and β_{3s} appear in Eqs. (B1)–(B8). All these force constants are multiplied by a factor of 4 or 8. As a result, even a small change in these force constants is magnified by a factor of 4 or 8, and such a behavior is indeed observed in the full surface dynamics. Also note that α_{2s} and α_{3s} appear only in the dispersion of the $SP_\parallel$ modes (the expression for the SH modes are not taken into consideration, since these modes are not measured). Thus it is possible to modify α_{2s}, α_{3s}, β_{2s}, and β_{3s} in such a way as to simultaneously raise $SP_\perp$ and lower $SP_\parallel$ to obtain agreement with experiment. This analysis shows, in addition, that there could be small changes in α_1 and β_1 between the surface and the second layer, but the experimental data do not enable us to determine these changes with any certainty. Similarly, there could be surface-related changes in the charge-fluctuation parameters. However, as mentioned earlier, the influence of these changes on the surface modes is small, and therefore they cannot be determined unambiguously. We have kept the charge-fluctuation parameters at the surface at their bulk values.

C. Surface modes at 900 K

The calculated dispersion curves of the surface modes $SP_\parallel$ (solid lines), $SP_\perp$ (long-dashed lines), and SH (short-dashed lines) along $\bar{\Gamma}\bar{X}$ and $\bar{\Gamma}\bar{M}$ are shown in Fig. 6(a). The lower bulk band edges are seen to exhibit a parabola-

TABLE II. Force constants (in THz^2) at the surface of the Nb(001) slab. Only those force constants that are changed from their bulk values are listed. The subscript s denotes that the force constants are *in* the surface layer.

$\alpha_{2s}=1.6M$	$\beta_{2s}=-0.8M$
$\alpha_{3s}=0.4M$	$\beta_{3s}=0.0$

like increase in the neighborhood of $\bar{\Gamma}$. Along $\bar{\Gamma}\bar{X}$ the SH and $SP_\perp$ modes lie very close to each other, while $SP_\parallel$ lies in the bulk band as a resonance. Along $\bar{\Gamma}\bar{M}$ the $SP_\parallel$ resonance becomes weak for $Q > 0.7$ Å^{-1} and ceases to exist at $Q \approx 0.8$ Å^{-1}. Hence it is shown as a dashed line (two dashes) in this region, namely, $0.7 < Q < 0.8$ Å^{-1}. At $Q = 0.65$ Å^{-1} a well-localized $SP_\parallel$ surface mode appears in the bulk band; it emerges from the bulk band at $Q = 0.75$ Å^{-1}. For $Q > 0.94$ Å^{-1}, the $SP_\parallel$ and $SP_\perp$ modes interchange their vibrational character. Hence, for $Q > 0.94$ Å^{-1}, the lower mode is shown as a solid line and the upper mode is shown as a dashed line. Such an interchange is not observed along $\bar{\Gamma}\bar{X}$. However, along both directions, both modes have mixed character; i.e., the vibration in $SP_\parallel$ is *predominantly* longitudinal and in $SP_\perp$ it is *predominantly* perpendicular to the Nb(001) plane.

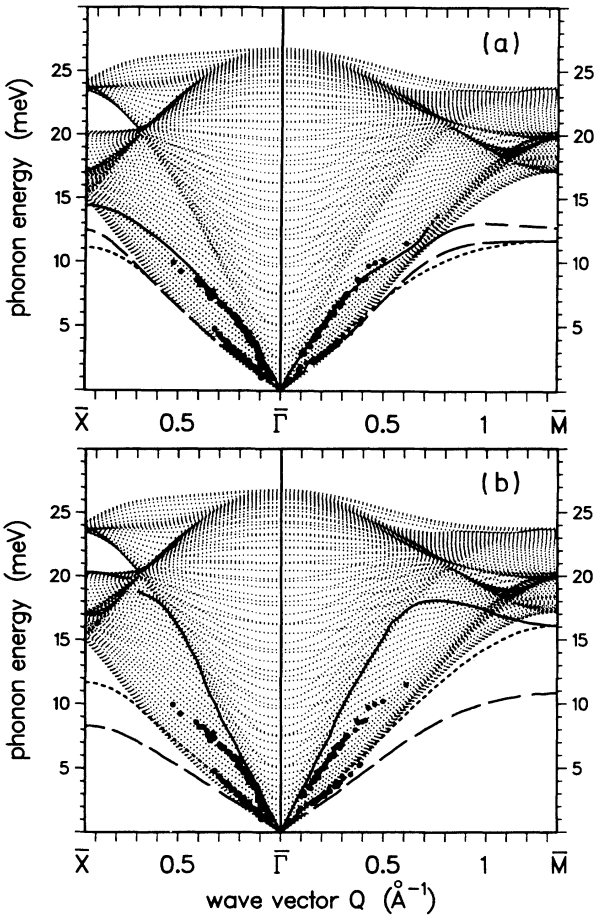

FIG. 6. (a) Measured and calculated surface phonons and resonances of Nb(001) along the symmetry directions [100] ($\bar{\Gamma}\bar{X}$) and [110] ($\bar{\Gamma}\bar{M}$). The closed circles represent our experimental data at 900 K. The theoretical dispersion curves are determined from the dynamics of a 51-layer Nb(001) slab, with the bulk and surface force constants given in Tables I and II, respectively. The solid lines represent the surface phonons and resonances having mainly longitudinal ($SP_\parallel$) polarization. The lines with long dashes correspond to the surface phonons having polarization mainly perpendicular to the Nb(001) surface ($SP_\perp$ modes), and those with short dashes denote the shear horizontal (SH) surface modes. The dotted lines represent the bulk modes of the 51-layer slab. For clarity, only a half of the 153 bulk modes (alternate dispersion curves) are drawn. (b) Same as in (a) except that the force constants at the Nb(001) surface are taken to be the same as their bulk counterparts (dynamics of the truncated bulk). A comparison of this figure with (a) shows the effect of the force constants in Table II on the surface modes and resonances.

Note that the measured $SP_\perp$ mode along $\bar{\Gamma}\bar{M}$ and the measured $SP_\parallel$ resonance along both directions can be fitted quite well. Along $\bar{\Gamma}\bar{X}$ the agreement for the $SP_\perp$ mode is not satisfactory. However, inclusion of all the charge-fluctuation parameters of Allen[9] will not solve this problem, since the charge-fluctuation parameters do not affect the nature of the surface modes appreciably. In other words, the discrepancy in $SP_\perp$ along $\bar{\Gamma}\bar{X}$ apparently points to a shortcoming of the underlying bulk model. This is a significant observation since, judged on the basis of the bulk phonons alone, the bulk model seems to be quite adequate. This is a clear example of the fact that surface modes can reveal the shortcomings of a bulk model because of the broken symmetry at the surface.

V. SUMMARY

Using helium-atom scattering we have measured the surface phonon dispersion of the Nb(001) surface in both high-symmetry directions. Two distinct phonon modes are clearly resolved, which have been identified as the Rayleigh mode and a longitudinal resonance at higher phonon energies. This ordering in energy is typical for a stable metal surface. No phonon anomalies could be found within the accessible wave-vector range. In particular, the parabolalike increase in the transverse bulk phonon-dispersion curves close to Γ does not show up for the corresponding surface modes. We were unable to detect phonon inelastic scattering from the two surface modes for wave vectors in the second half of the surface Brillouin zone. The reason for this behavior could be that the inelastic cross section becomes unfavorable. It cannot, however, be ruled out that experimental limitations due to problems in maintaining a clean Nb(001) surface for a sufficiently long measuring time are responsible for the apparent vanishing of the surface modes for large wave vectors.

We have constructed a lattice-dynamical model that includes the usual central and angular forces as well as electronic degrees of freedom. This model is capable of describing the experimental data, both in the bulk and at the (001) surface. However, the modifications of the surface force constants with respect to the corresponding bulk values are quite large, and even then the calculated $SP_\perp$ mode along $\bar{\Gamma}\bar{X}$ does not agree fully with the experimental data [cf. Fig. 6(a)]. This discrepancy reveals the limits of applicability of the force-constant models to surface dynamics. Moreover, our analysis also demonstrates that a model that describes the bulk phonon dispersion well does not suffice to reproduce the details of surface phonon dispersion. A satisfactory description of the sur-

face phonons will probably have to be based on a first-principles approach.

ACKNOWLEDGMENTS

We would like to thank K. Schulze for providing the niobium single crystal. This work was partially supported by the National Science Foundation through Grant No. DMR-8816301 and by the Robert A. Welch Foundation through Grant No. F-433. Acknowledgment is also made to the donors of the Petroleum Research Fund, administered by the American Chemical Society, for partial support of this research.

APPENDIX A: CHARGE-FLUCTUATION MODEL FOR A SLAB

The charge-fluctuation model was formulated by Allen[9] for one particle per unit cell. In order to apply it to a slab, it needs to be generalized for a multiparticle basis. Such a generalization, applicable for a lattice in two or three dimensions, is outlined here. We start with Eq. (3) of Ref. 9, which gives the charge-fluctuation part of the Hamiltonian for one particle per unit cell:

$$H_1=\sum_{L,l,R}\sum_{\alpha,\beta}\rho_{L\alpha}(l)A^{L}_{\alpha\beta}(R)u_\beta(l+R) + \tfrac{1}{2}\sum_{L,L'}\sum_{l,R}\sum_{\alpha,\beta}\rho_{L\alpha}(l)\Phi^{LL'}_{\alpha\beta}(R)\rho_{L'\beta}(l+R)\ , \quad \text{(A1)}$$

where l denotes the lattice points, R the lattice vectors, $u_\alpha(l)$ the αth Cartesian component of the displacement of the lth atom, and $\rho_{L\alpha}(l)$ the charge-fluctuation (electronic) coordinates having Cartesian components α and symmetry L (cf. Ref. 9 for details). $A^{L}_{\alpha\beta}(R)$ and $\Phi^{LL'}_{\alpha\beta}(R)$ are phenomenological coupling constants between a charge fluctuation and a displacement and between two charge fluctuations, respectively.

In order to generalize Eq. (A1) for a multiparticle basis, we write it in an equivalent form as follows:

$$H_1=\rho_L(l;\alpha)A^{L}(l'-l;\alpha,\beta)u(l';\beta) + \tfrac{1}{2}\rho_L(l;\alpha)\Phi^{LL'}(l'-l;\alpha,\beta)\rho_{L'}(l';\beta)\ . \quad \text{(A2)}$$

Here and hereafter *we assume summation over repeated indices* unless stated otherwise. Now replace the lattice points l and l' by l,k and l',k', respectively, where k and k' denote the basis. Then H_1 can be generalized as

$$H_1=\rho_L(l;k\alpha)A^{L}(l'-l;k\alpha,k'\beta)u(l';k'\beta) + \tfrac{1}{2}\rho_L(l;k\alpha)\Phi^{LL'}(l'-l;k\alpha,k'\beta)\rho_{L'}(l';k'\beta)\ . \quad \text{(A3)}$$

Since the second term in Eq. (A3) is a quadratic form, we can assume without any loss of generality that the matrix $\Phi^{LL'}$ is symmetric; i.e.,

$$\Phi^{LL'}(l'-l;k\alpha,k'\beta)=\Phi^{L'L}(l-l';k'\beta,k\alpha)\ . \quad \text{(A4)}$$

The equations of motion associated with H_1 can now be obtained immediately:

$$\frac{\partial H_1}{\partial u(l;k\alpha)}=\rho_{L'}(l';k'\beta)A^{L'}(l-l';k'\beta,k\alpha) \quad \text{(A5)}$$

and

$$\frac{\partial H_1}{\partial \rho_L(l;k\alpha)}=A^{L}(l'-l;k\alpha,k'\beta)u(l';k'\beta) + \Phi^{LL'}(l'-l;k\alpha,k'\beta)\rho_{L'}(l';k'\beta)=0\ . \quad \text{(A6)}$$

The right-hand side of Eq. (A6) is zero due to the adiabatic approximation [cf. Eq. (4) of Ref. 9]. Assuming plane-wave solutions to these equations, namely,

$$u(l';k'\beta)=u_q(k'\beta)\exp[iq(l'-l)] \quad \text{(A7)}$$

and

$$\rho_{L'}(l';k'\beta)=\rho_{L'q}(k'\beta)\exp[iq(l'-l)]\ , \quad \text{(A8)}$$

we obtain

$$\frac{\partial H_1}{\partial u(l;k\alpha)}=\rho_{L'q}(k'\beta)A^{L'}_{-q}(k'\beta,k\alpha) \quad \text{(A9)}$$

and

$$0=A^{L}_{q}(k\alpha,k'\beta)u_q(k'\beta)+\Phi^{LL'}_{q}(k\alpha,k'\beta)\rho_{L'q}(k'\beta)\ , \quad \text{(A10)}$$

where A^{L}_{q} and $\Phi^{LL'}_{q}$ are defined by

$$A^{L}_{q}(k\alpha,k'\beta)=A^{L}(l';k\alpha,k'\beta)\exp(iql') \quad \text{(A11)}$$

and

$$\Phi^{LL'}_{q}(k\alpha,k'\beta)=\Phi^{LL'}(l';k\alpha,k'\beta)\exp(iql')\ . \quad \text{(A12)}$$

Here and hereafter no sum over q is implied. Equation (A10) can be solved for $\rho_{L'q}(k'\beta)$. Then Eq. (A9) yields

$$\frac{\partial H_1}{\partial u(l;k\alpha)}=-(A^{L'}_{q})^{\dagger}(k\alpha,k'\beta)(\Phi^{-1}_{q})^{L'L''}(k'\beta,k''\sigma) \times A^{L''}_{q}(k''\sigma,k'''\nu)u_q(k'''\nu)\ . \quad \text{(A13)}$$

Thus the contribution of H_1 to the dynamical matrix, denoted by $D^{(1)}_{q}(k\alpha,k'\beta)$, is

$$D^{(1)}_{q}(k\alpha,k'\beta)=-(A^{L''}_{q})^{\dagger}(k\alpha,k''\sigma) \times(\Phi^{-1}_{q})^{L''L'''}(k''\sigma,k'''\nu)A^{L'''}_{q}(k'''\nu,k'\beta)\ . \quad \text{(A14)}$$

Note that the above analysis is valid for a lattice in three as well as in two dimensions; i.e., also for a slab.

Next we derive a sufficient condition for the translational invariance of the dynamical matrix. Since the non-charge-fluctuations part of the dynamical matrix satisfies the translational invariance, the charge-fluctuations part must be translationally invariant independently; i.e., we must have

$$\sum_{k}D^{(1)}_{0}(k\alpha,k'\beta)=\sum_{k'}D^{(1)}_{0}(k\alpha,k'\beta)=0\ . \quad \text{(A15)}$$

In view of Eqs. (A14) and (A15), we see that the following

condition is sufficient to establish translational invariance:

$$\sum_k A_0^{L''}(k''\sigma,k\alpha)=\sum_k \sum_{l-l''} A^{L''}(l-l'';k''\sigma,k\alpha)=0 \tag{A16}$$

for every L'', k'', σ, and α. This condition can be stated in words as follows: For every row of each one of the matrices $A_0^{L''}$ indexed by the superscript L'', the sum of every third element (corresponding to $\alpha=x,y,z$) must vanish. We have used this condition to ensure the translational invariance of the Nb(001) slab.

In our lattice-dynamical model of Nb(001) we include, (i) scalar ($L=1$) interaction Φ^{11} up to second neighbors, which yields parameters ϕ_1 and ϕ_2, (ii) on-site (zeroth-neighbor) quadrupolar ($L=25'$) interaction $\Phi^{25'25'}(l'-l;k\alpha,k'\beta)=\delta_{ll'}\delta_{kk'}\delta_{\alpha\beta}$, i.e., no free parameters, (iii) scalar ($L=1$) interaction A^1 up to second neighbors, which yields parameters A_1 and A_2, and (iv) quadrupolar ($L=25'$) interaction $A^{25'}$ up to first neighbors, giving two parameters B_{1a} and B_{1b} (see Table I of Ref. 9 for details). With the use of these parameters in Eq. (A14), the contribution of charge fluctuations to the dynamical matrix of the Nb(001) slab is calculated.

APPENDIX B: ESTIMATES OF SURFACE-MODE DISPERSIONS

In this appendix we present analytical expressions for the dispersion of the Rayleigh ($SP_\perp$), longitudinal ($SP_\parallel$), and shear horizontal (SH) modes of an unreconstructed bcc (001) slab, in an approximation in which only the atoms in the surface layer are allowed to vibrate, while those in the second and subsequent layers remain stationary. These expressions are reproduced from our earlier work on W(001) (Ref. 15) and do not incorporate the charge-fluctuation parameters. Along $\bar{\Gamma}\bar{X}$,

$$M\omega^2_{SP_\perp}(q)=C_1+4(\beta_{2s}+2\beta_{3s}-\tfrac{4}{9}\chi_1)\sin^2(qa_0/2)\ , \tag{B1}$$

$$M\omega^2_{SP_\parallel}(q)=C_2+4(\alpha_{2s}+\alpha_{3s}+\beta_{3s}+\tfrac{16}{9}\chi_1)\sin^2(qa_0/2)\ , \tag{B2}$$

$$M\omega^2_{SH}(q)=C_2+4(\beta_{2s}+\alpha_{3s}+\beta_{3s}-\tfrac{4}{9}\chi_1)\sin^2(qa_0/2)\ , \tag{B3}$$

and along $\bar{\Gamma}\bar{M}$,

$$M\omega^2_{SP_\perp}(q)=C_1+8(\beta_{2s}-\tfrac{4}{9}\chi_1)\sin^2(qa_0/2)+4\beta_{3s}\sin^2(qa_0)\ , \tag{B4}$$

$$M\omega^2_{SP_\parallel}(q)=C_2+4(\alpha_{2s}+\beta_{2s}+\tfrac{12}{9}\chi_1)\sin^2(qa_0/2)+4\alpha_{3s}\sin^2(qa_0)\ , \tag{B5}$$

$$M\omega^2_{SH}(q)=C_2+4(\alpha_{2s}+\beta_{2s}+\tfrac{12}{9}\chi_1)\sin^2(qa_0/2)+4\beta_{3s}\sin^2(qa_0)\ , \tag{B6}$$

where M is the mass of the niobium atom, a_0 is the bulk lattice constant of niobium, $0\le qa_0\le\pi$ along *both* directions, and α_{is},β_{is} ($i=2,3$) are the ith-neighbor interactions among the surface atoms. Here C_1 and C_2 are given by

$$C_1=\tfrac{4}{3}(\alpha_1+2\beta_1)+\alpha_2+2\alpha_3+2\beta_3+\tfrac{96}{9}\chi_1\ , \tag{B7}$$

$$C_2=\tfrac{4}{3}(\alpha_1+2\beta_1)+\beta_2+\alpha_3+3\beta_3+\tfrac{40}{9}\chi_1\ . \tag{B8}$$

[1] K. Yonehara and L. D. Schmidt, Surf. Sci. **25**, 238 (1971); M. K. Debe and D. A. King, J. Phys. C **10**, L203 (1977).

[2] T. E. Felter, R. A. Barker, and P. J. Estrup, Phys. Rev. Lett. **38**, 1138 (1977).

[3] A. J. Melmed, S. T. Ceyer, R. T. Tung, and W. R. Graham, Surf. Sci. **111**, L701 (1981).

[4] A. Titov and W. Moritz, Surf. Sci. **123**, L709 (1982).

[5] Y. Nakagawa and A. D. B. Woods, in *Lattice Dynamics*, edited by R. F. Wallis (Pergamon, Oxford, 1965), p. 39; Phys. Rev. Lett. **11**, 271 (1963).

[6] P. H. Dederichs, H. Schober, and D. J. Sellmeyer, in *Numerical Data and Functional Relationships in Science and Technology*, Landolt Börnstein, New Series, edited by K. H. Hellwege and J. L. Olson, Group III, Vol. 13a (Springer, Berlin, 1981), p. 96.

[7] C. M. Varma and W. Weber, Phys. Rev. Lett. **39**, 1094 (1977); Phys. Rev. B **19**, 6142 (1979).

[8] N. Wakabayashi, Solid State Commun. **23**,737 (1977).

[9] P. B. Allen, Phys. Rev. B **16**, 5139 (1977).

[10] G. Brusdeylins, R. B. Doak, and J. P. Toennies, Phys. Rev. B **27**, 3662 (1983).

[11] *Hydrogen in Metals*, edited by G. Alefeld and J. Volkl (Springer, New York, 1978).

[12] Y. Li, J. L. Erskine, and A. C. Diebold, Phys. Rev. B **34**, 5951 (1986).

[13] B. S. Fang, C. A. Ballentine, and J. L. Erskine, Surf. Sci. **204**, L713 (1988).

[14] A. D. Kulkarni and F. W. de Wette, Surf. Sci. **186**, 469 (1987).

[15] A. D. Kulkarni, F. W. de Wette, and J. Prade, J. Electron Spectrosc. Relat. Phenom. **44**, 397 (1987).

[16] M. Born and K. Huang, *Dynamical Theory of Crystal Lattices* (Clarendon, Oxford, 1954).

[17] D. I. Bolef, J. Appl. Phys. **32**, 100 (1961).

[18] H. Bilz, D. Strauch, and R. K. Wehner, in *Encyclopedia of Physics: Vol. XXV/2d, Light and Matter Id*, edited by L. Genzel (Springer, Berlin, 1984), p. 35.

[19] It would appear from Fig. 6(b) that the lower measured dispersion curve may be due to the bulk band edge, particularly along $\bar{\Gamma}\bar{M}$, where it even seems to duplicate the parabolalike increase of the bulk band edge. However, our surface-projected density-of-states calculations show no appreciable contribution due to the bulk band edge, thus ruling out this interpretation.